

Investigating and improving methods for determining the kinematics of solar eruptive events.

J. P. Byrne¹, D. M. Long², P. T. Gallagher³, D. S. Bloomfield³, S. A. Maloney⁴, R. T. J. McAteer⁵, H. Morgan⁶, and S. R. Habbal¹

¹ Institute for Astronomy, University of Hawai'i, 2680 Woodlawn Drive, Honolulu, HI 96822, USA.
e-mail: jbyrne@ifa.hawaii.edu

² UCL–Mullard Space Science Laboratory, Holmbury St. Mary, Dorking, Surrey, RH5 6NT, UK.

³ School of Physics, Trinity College Dublin, College Green, Dublin 2, Ireland.

⁴ Skytek, 51/52 Fitzwilliam Square West, Dublin 2, Ireland

⁵ Department of Astronomy, New Mexico State University, Las Cruces, NM 88003-8001, USA.

⁶ Institute of Mathematics and Physics, Aberystwyth University, Ceredigion, SY23 3BZ, UK.

Received ?; accepted ?

ABSTRACT

Context. The study of solar eruptive phenomena is of great importance in the context of solar and heliophysics and space weather. Coronal mass ejections and coronal waves are specifically energetic manifestations of the restructuring of solar magnetic field alongside mass motion of the plasma. Characterising this motion is vital for deriving the dynamics of these events, in order to understand the physics driving their occurrence and propagation. Thus the development and use of appropriate numerical methods for measuring event kinematics is imperative.

Aims. In this paper we show that traditional techniques for the determination of CME and “EIT wave” kinematics, as currently applied, do not return accurate estimates of the true kinematics of the feature. We highlight the errors inherent in these approaches and illustrate a recipe for accurate estimates of the kinematics using a residual resampling bootstrapping approach to determine the confidence interval associated with the model used to measure them.

Methods. We discuss the errors inherent in the use of numerical differentiation techniques when applied to small data-sets. We present a residual resampling bootstrapping approach as a statistically rigorous technique for the determination of accurate kinematic estimates.

Results. It is shown that accurate feature kinematics can only be estimated by applying a pre-determined model to the position measurements. The validity of this model must be based on the physical properties of the feature that are to be measured, and the accuracy of applying that model to the data can be examined using a bootstrapping approach to determine the confidence interval associated with the estimated model parameters.

Conclusions. Improved methods for determining the kinematics of solar eruptive events are demonstrated to great effect, overcoming many issues highlighted in traditional numerical differencing and error propagation techniques.

Key words. Sun: activity – Sun: corona – Sun: coronal mass ejections (CMEs)

1. Introduction

The most defining feature of an eruptive solar event, such as a coronal mass ejection (CME) or a coronal wave (commonly called an “EIT Wave”), is its motion, which can be of direct consequence to space weather within the heliosphere. These generally fast-moving features, resulting from the release of magnetic energy on the surface of the sun, are observed to propagate across a sequence of solar-disk and corona images. Observational catalogues of both phenomena have been compiled over more than \sim 20 years of observations (e.g., Illing & Hundhausen, 1985; Yashiro et al., 2004; Thompson & Myers, 2009), with the physical properties of both phenomena extensively characterised (see the recent reviews by e.g., Gallagher & Long, 2011; Patsourakos & Vourlidas, 2012; Howard, 2011; Webb & Howard, 2012). Understanding the physics governing their eruption and propagation is therefore extremely important if scientists are ever to become skilled at predicting their behavior.

As transient phenomena, the kinematics of these eruptive events continue to be one of the most important characteristics used to classify them. The motion of the observed bulk plasma of each phenomena is traditionally identified using difference images, where a preceding image is subtracted from a leading image to highlight moving features. However, this approach enhances relative rather than actual motion, and is prone to spatiotemporal crosstalk and user-dependent bias. More recent work has used single image processing techniques such as wavelet transforms (Byrne et al., 2009; Morgan et al., 2012) and automated approaches (e.g., Long et al., 2011; Byrne et al., 2012; Podladchikova et al., 2012) to overcome these errors and reveal the true physical characteristics of the features. Thus by accurately tracking the position of a feature with time it is possible to determine its kinematics, allowing an insight into the physical properties of the phenomenon.

The kinematics of these features are important for a variety of reasons. The true physical nature of coronal waves is not fully understood, with two main competing theories:

that they are waves (e.g., [Shen & Liu, 2012](#); [Veronig et al., 2010](#)) or signatures of magnetic field restructuring during a CME eruption (e.g., [Schrijver et al., 2011](#); [Chen & Wu, 2011](#)). The kinematics of coronal waves have been proposed as one of the main discriminators between these competing theories, with the relatively high velocities measured thus far for this phenomenon suggesting a wave interpretation may be appropriate (cf. [Warmuth & Mann, 2011](#); [Zheng et al., 2012](#)). Similarly, CME kinematics are vitally important from a space weather point of view as they allow increased accuracy in the predicted arrival time of the feature at Earth and elsewhere throughout the heliosphere ([Byrne et al., 2010](#); [Schwenn et al., 2005](#); [Prangé et al., 2004](#)). The kinematic behaviour of the CME in the low solar corona may also be used to discriminate between eruption mechanisms ([Lin et al., 2010](#)). However [Wen et al. \(2007\)](#) demonstrate that the errors in CME acceleration values can be of the same order as the accelerations typically measured, making this task difficult.

A variety of different mathematical techniques exist for deriving the kinematics of transient features, most being based upon some form of numerical differentiation of the distance-time measurements, and/or the fitting of a pre-assumed model function. While such techniques may be mathematically sound, some of them are not necessarily applicable to the derivation of kinematics for these features and can produce spurious results. A recapitulation of standard numerical methods and error propagation are presented in Section 2. Simulations of the drawbacks of a standard numerical derivative are presented in Section 3. In Section 4 we outline a more appropriate method for inspecting the kinematics of CMEs and coronal waves, as applied to model data. In Section 5 some real-data cases are inspected via these methods, and motivate the proposed treatment of data from the new coronal image processing CME catalogue (CORIMP; [Morgan et al., 2012](#); [Byrne et al., 2012](#)), and coronal pulse identification and tracking algorithm catalogue (CORPITA; [Long et al., 2011](#)). The main conclusion are reiterated in Section 6.

2. Numerical Differentiation & Error Propagation (recapitulation)

When presented with a moving object through a sequence of image frames such that it is possible to measure its position at each time step, the technique of numerical differentiation is often used to derive the velocity and acceleration of the object. In the standard 2-point approach, it should be possible to derive the time evolution of a system at time step $t + \delta t$ according to the system values at time step t . This may be applied through the technique of forward, reverse or centre differencing, resulting in an estimate of the speed of the object at a specific time step given its positional information. More commonly, a 3-point Lagrangian interpolation is applied to better approximate the kinematics of a moving object by solving for the Lagrange polynomials that best fit across three datapoints (e.g. DERIV.PRO in IDL). Each of these schemes is based upon the Taylor series expansion of a real function $f(t)$:

$$f(t_0 + \delta t) = f(t_0) + f'(t_0)\delta t + \frac{f''(t_0)}{2!}(\delta t)^2 + \dots \quad (1)$$

but due to the approximation of an infinite series with a finite number of terms and iterations, an error must be as-

sociated with the result, based on its deviation from the true solution. Generally the Euler method is employed, using the formula:

$$y_{n+1} = y_n + h f(t_n, y_n) \quad (2)$$

to solve the initial value problem $y' = f(t, y)$ given $y(t_0) = y_0$, where h is the stepsize such that $t_n = t_0 + nh$. The convergence of such an approximation to the actual solution is prone to two sources of error: truncation error (the difference between the true solution and the approximation), and round-off error (the limited precision of the approximation). Added to this is the fact that the data measurements themselves are subject to uncertainties in both the positional and temporal information, and the ability of the numerical differentiation techniques to derive kinematics becomes highly jeopardised, as shall be shown.

Given a function $x = f(u, v)$, the error propagation equation (based on the standard deviations σ of the variables) is written:

$$\sigma_x^2 = \sigma_u^2 \left(\frac{\partial x}{\partial u} \right)^2 + \sigma_v^2 \left(\frac{\partial x}{\partial v} \right)^2 + 2\sigma_{uv}^2 \left(\frac{\partial x}{\partial u} \right) \left(\frac{\partial x}{\partial v} \right) + \dots \quad (3)$$

Specifically in the case of kinematic analyses, this is used to propagate the errors on the distance-time data $r(t)$ into the velocity $v(t)$ and acceleration $a(t)$ profiles to determine the associated uncertainties. In the case of distance-time data the covariance terms are deemed to be zero because the quantities are uncorrelated.

When presented with relatively low sampling of the data, as in the case of CME and coronal wave observations, it is generally found that the simplest differentiation techniques are not applicable. The forward and/or reverse differencing techniques act to shift the kinematic profiles by one time-step, which is substantial enough to be of concern here (i.e., they derive a result at the current time-step, based on the pro/preceding time-step). Centre differencing employs the two neighbouring data-points of the point under examination, and so is a better indication of the result at that time-step, but it fails at both endpoints. In any case these should not be employed when the spacing of the data-points is unequal, i.e., when the cadence δt is not constant. Therefore the 3-point Lagrangian interpolation technique is often used (which gives the same result as the centre-difference otherwise, but includes the endpoints and has an associated error propagation formulation). The Lagrangian interpolation polynomial is given by:

$$L(x) = \sum_{j=0}^2 y_j l_j(x) \quad (4)$$

$$\text{where } l_j(x) = \prod_{i=0, i \neq j}^2 \frac{x - x_i}{x_j - x_i} \quad (5)$$

The derivative at point x is given by $L' = \partial_x L(x)$. So for the case of distance-time data being used to derive velocity (and similarly acceleration) the associated error is given by:

$$\sigma_{v_1}^2 = \frac{\sigma_{r(t_2)}^2 + \sigma_{r(t_0)}^2}{(t_2 - t_0)^2} + v^2 \left(\frac{\sigma_{t_2}^2 + \sigma_{t_0}^2}{(t_2 - t_0)^2} \right) \quad (6)$$

(as in DERIVSIG.PRO in IDL). The endpoint errors are derived from a weighting of the pro/preceding two data-points, that is therefore larger to reflect the unknown nature of the trend beyond the sample points.

Although the 3-point Lagrangian is mathematically sound, its application to solar eruptive event kinematics proves problematic. The main drawbacks are two-fold:

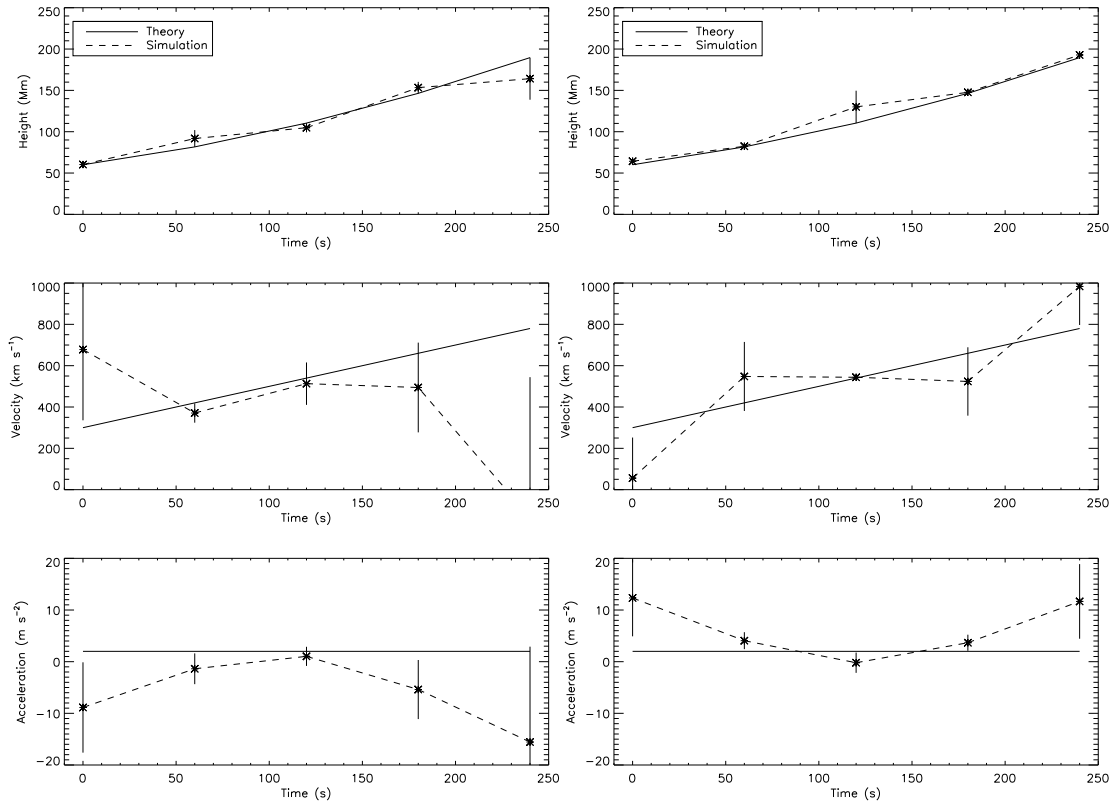


Fig. 1. A theoretical model for a CME with constant acceleration 2 m s^{-2} and initial velocity 300 km s^{-1} , and two simulations of how the resulting profiles for a noisy sample of data-points behave using 3-point Lagrangian interpolation.

1. The noise level, especially across low-cadence sampling, can scatter the measurements so that the numerical derivatives become untrustworthy and even misleading compared to the actual trends of the kinematic data.
2. The error-propagation formulation results in a misleading uncertainty interval on the velocity and acceleration profiles. For example, it counter-intuitively increases for increasing cadence measurements (that is, for larger observational time intervals).

3. Simulations

In the case of CMEs and coronal waves, there is great motivation to resolve the dynamics of their propagation as precisely as possible in order to study the forces at play. For example, CMEs in general may be undergoing continued driving (internal) forces, and positive or negative drag (external) forces. Similarly wave propagation may be affected by changes to the low-coronal environment, e.g., low-density coronal hole regions, or strong magnetic field active regions. Thus any changes to event acceleration that result from different phases of dominating force, and where or why this can occur, are of great interest. But the true kinematics of such events remains somewhat elusive given the inherent limitations of the data and the numerical methods employed. In our treatment of both phenomena here, we use cases of simulated CME and wave data interchangeably, to demonstrate both constant and non-constant acceleration profiles with varying scatter and cadence.

3.1. Effect of noisy scatter on deriving kinematics

As an example of the effect of scatter due to noisy data, we first simulate a simple height-time profile of a CME that propagates according to the quadratic equation:

$$r(t) = r_0 + v_0 t + \frac{1}{2} a t^2 \quad (7)$$

where $r_0 = 60 \text{ Mm}$ is the initial height, $v_0 = 300 \text{ km s}^{-1}$ is the initial velocity, and $a = 2 \text{ m s}^{-2}$ is the acceleration of the CME. Randomly generated scatter is applied to the height-time points to mimic noise on the data. The level of the noise is limited to values no greater than 20% of the corresponding idealized height at each time. An ‘extreme case’ errorbar on each datapoint is determined by its distance from the true height-time profile, to represent a scenario wherein all measurement uncertainties just manage to overlap the true profile. Various instances of randomized datapoint scatters result in erroneous trends in the velocity and acceleration profiles, even with the proper error treatment prescribed by the 3-point Lagrangian interpolation technique, and even in this simplest case of constant acceleration. Two examples are shown in the left and right of Figure 1 where completely opposing acceleration trends are determined for different samplings of the same dataset, indicating that the nature of the scatter in the samples is not satisfactorily reflected in the derived kinematics and their associated errorbars. At the very least the datapoints should be expected to overlap the truth in each plot so that it remains a valid solution. A possible assurance, even in the case of low-cadence samplings (or very fast events), is that instead of trusting the endpoints they simply be removed. Figure 1 would then show three datapoints for velocity and

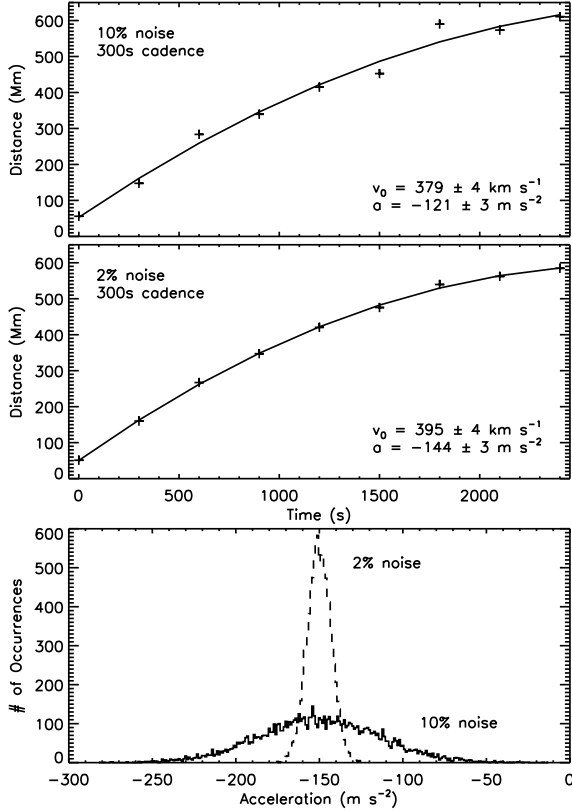


Fig. 2. Simulated datapoints for noise distributions with 3σ widths of $\pm 10\%$ (top), and $\pm 2\%$ (middle) of the model value, at a fixed cadence of 300s , and the resulting quadratic fit and v_0 and a parameters. The reduced noise level increases the precision in obtaining the true kinematics, as demonstrated by the different distributions of derived accelerations (bottom).

one datapoint for acceleration, that would reduce the biased trends and imply a constant acceleration close to the true value. However, when dealing with low-number samples, it would be better not to have to remove datapoints.

The effects of varying scatter due to noise on the data of a coronal wave were also examined, demonstrated here for the case of a constant acceleration event. The wave motion is modeled by Equation 7, where $r_0 = 50\text{ Mm}$ is the initial distance of the wave from the source, $v_0 = 400\text{ km s}^{-1}$ is the initial velocity of the wave, and $a = -150\text{ m s}^{-2}$ is the acceleration of the wave. Figure 2 shows the derived kinematics for the simulated dataset with random noise added, shown here for 3σ limits of 10% (top panel) and 2% (middle panel). A second-order polynomial (quadratic) is then fit to each dataset to test how the noise level affects the precision of the derived kinematics, even in this idealized case of knowing the underlying form of the data. The increased noise level acts to smooth out the true kinematics, as demonstrated by the different distributions of derived accelerations (bottom panel).

3.2. Effect of sampling cadence on deriving kinematics

As an example of the effect of cadence, we first simulate again the constant-acceleration profile of a coronal wave

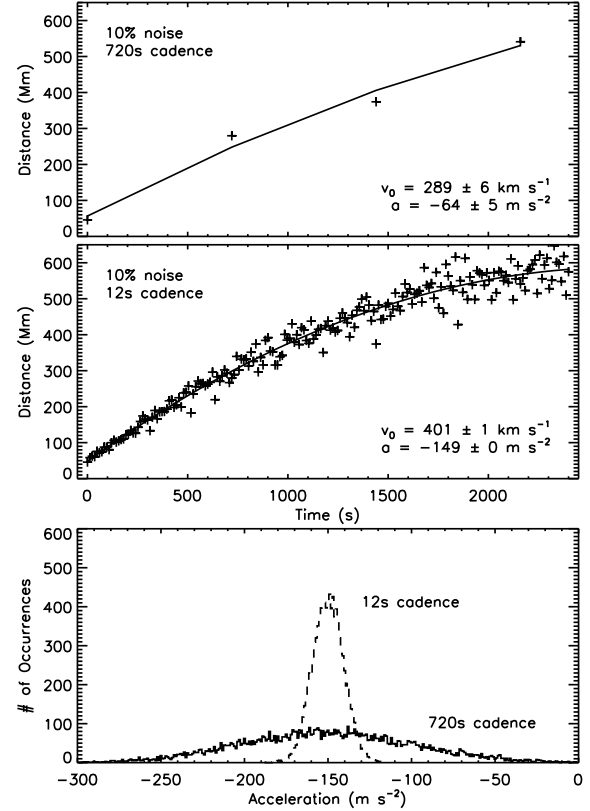


Fig. 3. Simulated datapoints for sampling cadences of 720s (EIT; top) and 12s (AIA; middle), at a fixed noise level of $\pm 10\%$, and the resulting quadratic fit and v_0 and a parameters. The increased cadence offers better precision in obtaining the true kinematics, as demonstrated by the different distributions of derived accelerations (bottom).

(as in Equation 7 and Figure 2). The data is sampled at cadences akin to the instruments EIT (12 mins) and AIA (12s), at a fixed noise level of 10%. Figure 3 shows examples of these, with a quadratic fit to the sample data to test the effect on the derived kinematics. It is clear that the higher-cadence data best resolves the true kinematic

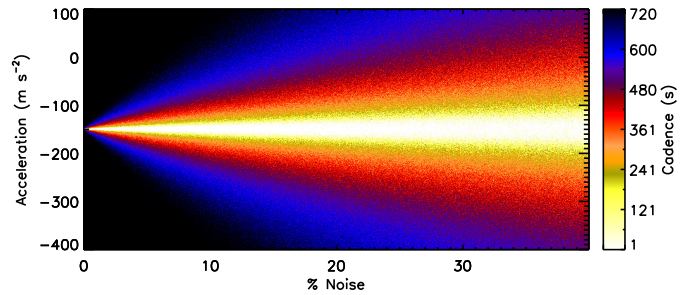


Fig. 4. A simulation of derived acceleration values, output from the model fit of Equation 7 (with examples shown in Figures 2 and 3), for varying noise levels of $0\text{--}40\%$ and varying cadence times of $1\text{--}720\text{s}$. As shown, both decreasing noise level and decreasing cadence time improves the chances of obtaining the correct acceleration value, being -150 m s^{-2} in this model coronal wave case.

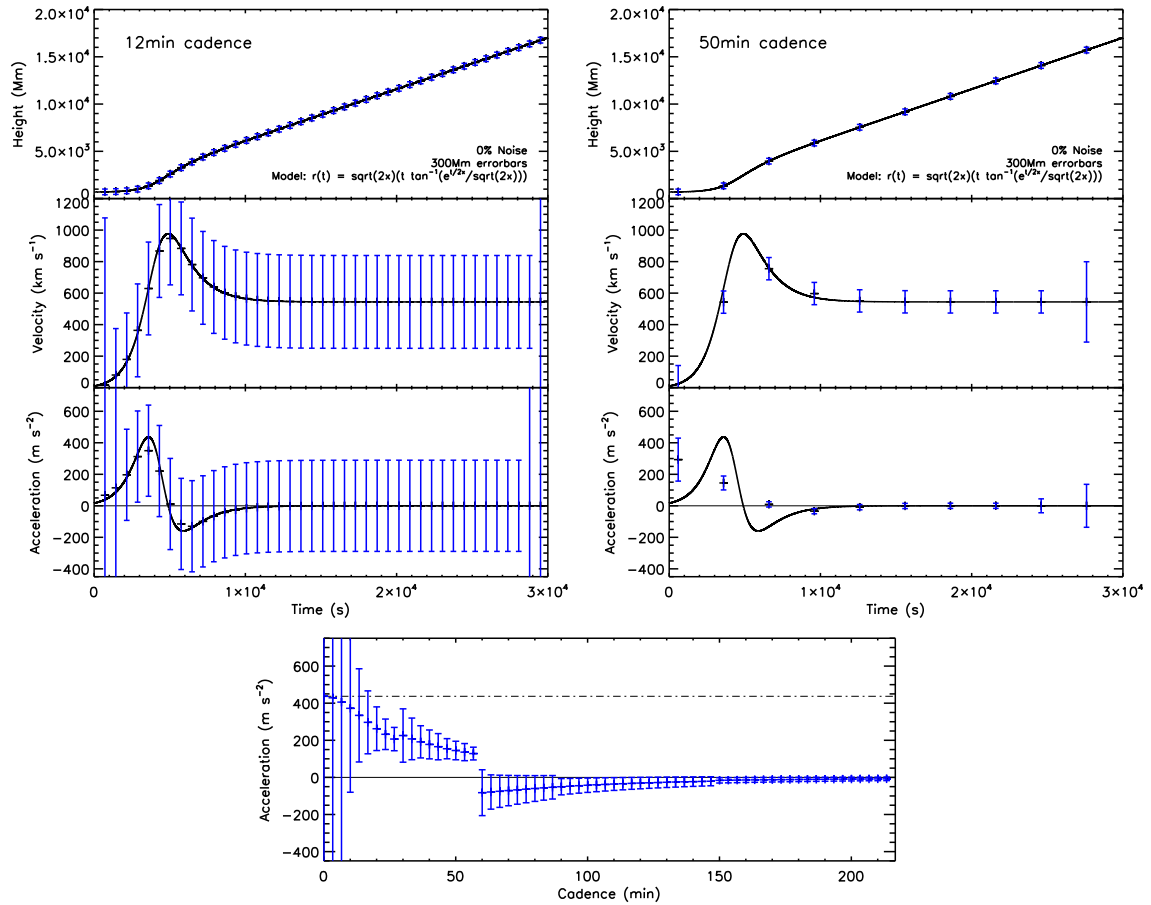


Fig. 5. A demonstration of the effects of cadence on the error propagation according to the 3-point Lagrangian interpolation. A theoretical model for a CME with non-constant acceleration peaking at 437 m s^{-2} is tested for varying cadences. The top left panels show the height, velocity and acceleration plots for data sampled at 12 minute cadence. The top right panels show similar for 50 minute cadence. Note how the error bars of the higher cadence data are counter-intuitively larger than the lower cadence data, even though the higher sampling rate better reveals the true kinematic trend. The bottom panel shows the derived peak acceleration against cadence, with the error bars reducing in magnitude (implying greater precision) even though the derived acceleration at lower cadence is less accurate.

profile, providing an accurate estimation of the wave velocity and acceleration. These results are consistent with the observations made by both Long et al. (2008) and Ma et al. (2009) and show that the effects of image cadence must be accounted for when trying to derive the true kinematics of a coronal wave.

In Figure 4 the combined effects outlined in Sections 3.1 and 3.2 are simulated for the model coronal wave case. The figure shows the result of plotting derived accelerations against all variations of noise from 0–40% at all variations of cadence from 1–720 s. Essentially the plots of the bottom panels of Figures 2 and 3 represent slices through the corresponding locations of Figure 4. Thus demonstrating that the reduction of both noise and cadence together is required to reduce the solution space (increase the accuracy) of the derived kinematics.

We next simulate a non-constant acceleration profile for a CME via the following equations (where the constant s is just a scaling factor):

$$h(t) = \sqrt{2s} t \tan^{-1} \left(\frac{e^{t/2s}}{\sqrt{2s}} \right) \quad (8)$$

$$v(t) = \sqrt{2s} \tan^{-1} \left(\frac{e^{t/2s}}{\sqrt{2s}} \right) + \frac{e^{t/2s} t}{e^{t/s} + 2s} \quad (9)$$

$$a(t) = \frac{e^{t/2s} (2s(t+4s) - e^{t/s}(t-4s))}{2s(e^{t/s} + 2s)^2} \quad (10)$$

The acceleration profile exhibits an initial peak followed by a deceleration and then leveling to zero. This is akin to a general impulsive CME that undergoes an initial high-acceleration eruptive phase, and then decelerates to match the solar wind speed during its propagation phase. Thus a model CME height-time profile is generated, enabling synthetic observation samples to be taken at different cadences (Figure 5).

We investigate the effect of the cadence of the observations on the derivation of the kinematics and associated errorbars using the standard 3-point Lagrangian interpolation. In the first instance fixed 3σ errorbars of $\pm 300 \text{ Mm}$ are applied to the height-time points, without any noise added. This is useful to simply test the effects of the cadence on the derived velocity and acceleration profiles and their associated errors. The top left and right plots of Figure 5 show the model height-time, velocity and acceleration profiles sampled at cadences of 12 and 50 minutes respectively. As the cadence is reduced, i.e., the time interval between observations is increased, the errorbars become smaller due to the inverse dependence of the Lagrangian error terms

on the time between the datapoints Δt^{-2} (see Equation 6). However, reducing the cadence reduces the resolution at which the acceleration peak is detectable, and so the acceleration profile is smoothed out. Conversely, the errorbars become erroneously large for very high-cadence measurements, even though the measurements better reveal the true trends of the kinematic profiles, as demonstrated in the bottom panel of Figure 5. This fundamentally implies that the errorbars do not truly reflect the uncertainty on the data at a given cadence, and are in fact redundant for these cases.

It is clear therefore, that the variation in both noise and imaging cadence can strongly influence the derived kinematics of a CME or coronal wave, and the 3-point Lagrangian technique does not return useful estimates of the associated uncertainty. However, it is possible to use other techniques along with a bootstrapping approach to overcome these issues, and produce a more statistically sound method for dealing with a small data sample.

4. Bootstrapping

When trying to determine an estimator for a particular parameter of interest and subsequently evaluate the accuracy of that estimator, a small sample size is immediately limiting. So techniques based on resampling methods have been developed, in order to approximate the behavior of the true distribution by resampling the data enough times to generate a maximum likelihood estimator of the distribution. Bootstrapping, first introduced by Efron (1979) and more recently described in e.g. Efron & Tibshirani (1994) and Chernick (1999), is one such technique, that may be formally defined as follows: Given a random sample of n independent identically distributed vectors $\mathbf{x} = (x_1, x_2, \dots, x_n)$ from an unknown probability distribution function \mathbf{F} and a real-valued estimator $\hat{\theta} = s(\mathbf{x})$, a procedure (the bootstrap) to assess the accuracy of $\hat{\theta}$ is defined in terms of the empirical distribution function $\hat{\mathbf{F}}$, which is the maximum likelihood estimator of the distribution for the observations when no parametric assumptions are made. Otherwise stated, a bootstrap sample $\mathbf{x}^* = (x_1^*, x_2^*, \dots, x_n^*)$ is generated by randomly sampling with replacement from the population of n objects, giving a resampled version of \mathbf{x} . The bootstrap algorithm then works by drawing many independent bootstrap samples, to estimate the standard error of $\hat{\theta}$ from the observed data \mathbf{x} .

Thus in the cases of CME and coronal wave observations, bootstrap techniques can prove very useful for determining the accuracy of the derived form of their kinematics. The implementation of the bootstrapping technique is as follows:

1. An initial fit to the data y is obtained, yielding the model fit \hat{y} with parameters \mathbf{p} .
2. The residuals of the fit are calculated: $\epsilon = y - \hat{y}$.
3. The residuals are randomly resampled with replacement to give ϵ^* .
4. The model is then fit to a new data vector $y^* = y + \epsilon^*$ and the parameters \mathbf{p}^* stored.
5. Steps 3–4 are repeated many times (e.g. 10,000).
6. Confidence intervals on the parameters are determined from the resulting distributions.

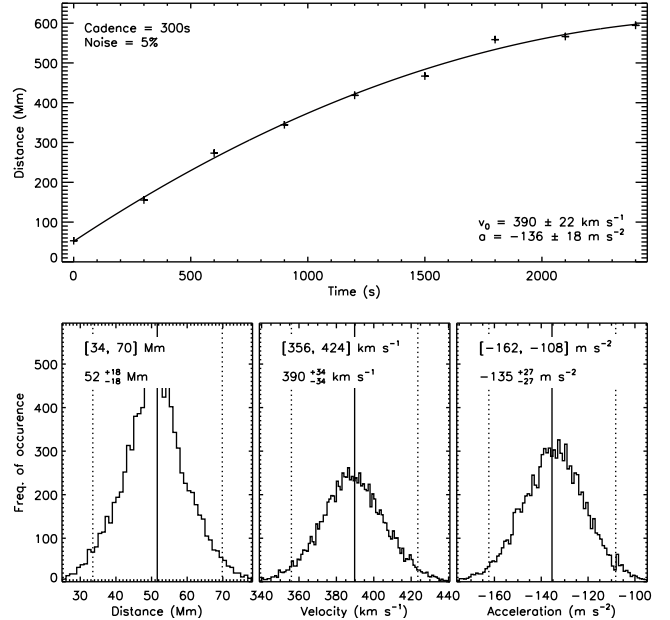


Fig. 6. Top panel shows the initial fit of Equation 7 to simulated coronal wave measurements with 5% noise and 300 s cadence. The fit parameters are quoted with 1-sigma uncertainties. The bottom panels show histograms of the initial distance, initial velocity, and acceleration values derived using the bootstrapping technique. The mean and 95% confidence interval are indicated by the solid and dotted lines respectively, and quoted on each panel in two ways (as a confidence interval, and as a mean with upper and lower bounds).

This technique was used to fit a quadratic model, first to the simulated coronal wave moving with constant acceleration (Equation 7), and second to the simulated CME moving with non-constant acceleration (Equation 10). In the case of the wave, the initial fit to the data and the bootstrapped distributions of initial height, initial velocity, and acceleration values are shown in Figure 6. Bootstrapping in this manner allows us to derive a confidence interval on the fit parameters. This is taken from the 100 α th and 100(1 – α)th percentiles of the distribution (giving a 95% confidence interval when $\alpha = .025$). Since in this case the distributions are close to symmetric about their means, we can see that the bootstrapped confidence interval is more precise than the corresponding uncertainty intervals on the single fit parameters. For example, the 1-sigma uncertainty on the acceleration given by the single fit in Figure 6 is $\pm 18 \text{ m s}^{-2}$, which is greater than half the 95% confidence interval range of $\pm 27 \text{ m s}^{-2}$ (i.e., likening the 95% range to a 2-sigma uncertainty).

However, bootstrapping of a model cannot be applied blindly, as we will demonstrate for a simple case of fitting the same constant acceleration form of Equation 7 to the non-constant acceleration of Equation 10. Figure 7 shows the associated model CME profile, sampled at 780 s cadence with 2% noise. The red points show the resulting distributions of velocity and acceleration values after the residuals are resampled with replacement. Thus a distribution of velocity and acceleration values are derived, with the corresponding median, interquartile range, and upper and lower fences overlaid

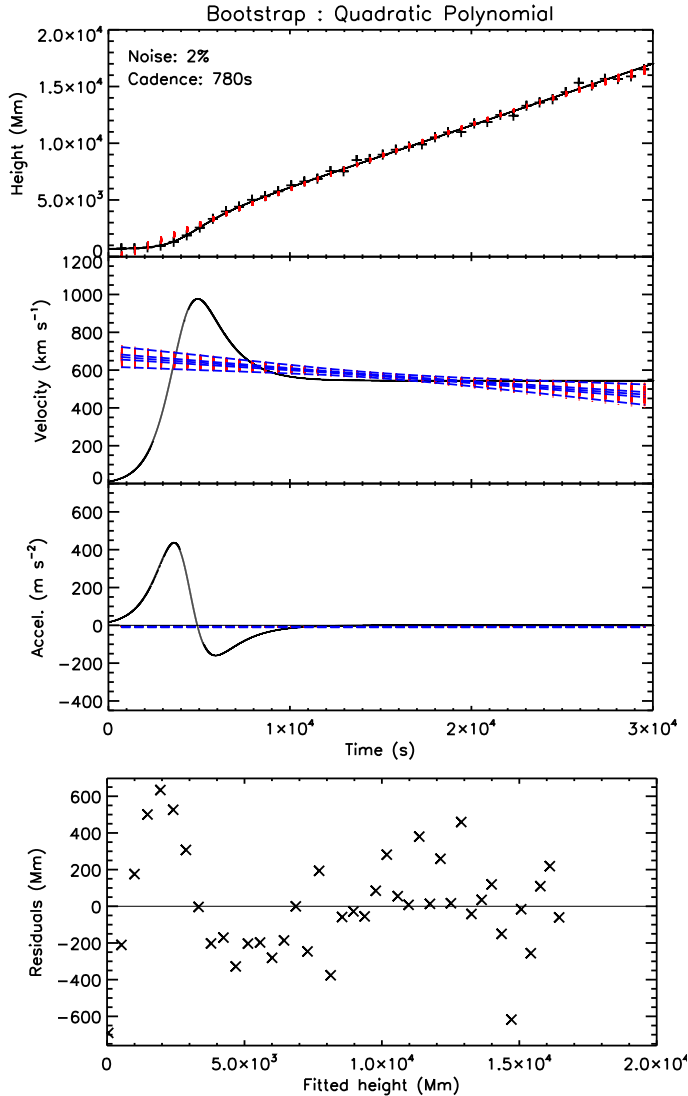


Fig. 7. The bootstrapped second order polynomial (quadratic) fit to simulated CME height-time data, with 2% noise and a sampling cadence of 780 s. The panels from top to bottom show the height, velocity, and acceleration plots, and the residuals of the initial fitted height. The red points show the resampled residuals with replacement, and the blue lines are the median, interquartiles range, and upper and lower fences on the bootstrapped fit. The quadratic form tends to smooth out the non-constant acceleration profile, as revealed by the trend in the residuals that indicates the fit is not appropriate for the data.

in blue. As expected, the second-order model is not appropriate to the true non-constant acceleration profile, as revealed by the trend in the residuals of the initial fit (bottom panel of Figure 7). So for any cases where possible non-constant acceleration profiles are to be revealed, the method for deriving the kinematics must be applied at an appropriate scale, and such that the residuals scatter randomly. In this specific case, the early acceleration peak is affecting the trend of the fit over the whole interval, when ideally a piecewise function should be used to characterize the different phases of motion. This is inspected in great detail by Schrijver et al. (2008) in an effort to model the early acceleration phase of erupting filaments involved in

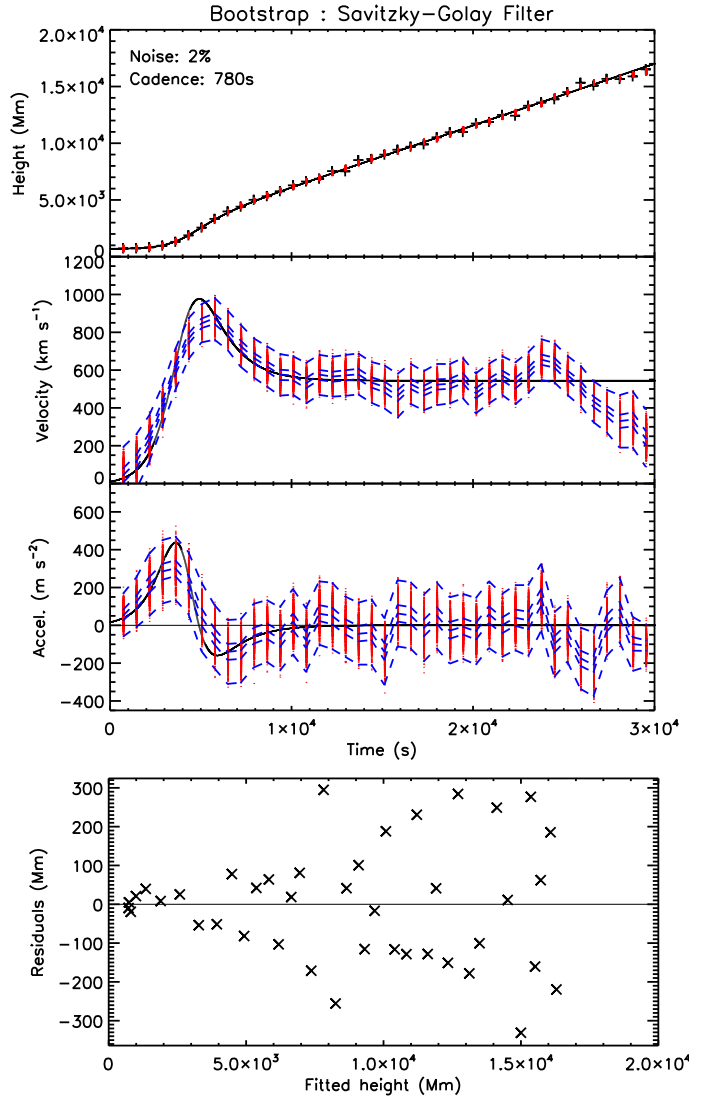


Fig. 8. The bootstrapped Savitzky-Golay filter method applied to the simulated CME height-time data as in Figure 7. This manner of piecewise fit smooths the data by fitting a polynomial to the three neighboring points either side of each datapoint, and is successful in revealing the non-constant acceleration profile. The randomly scattered residuals also indicate its appropriateness.

CMEs. They show that one functional form alone cannot describe the entire phase as well as a number of different functions can. Since we do not know the functional form that CME or coronal wave kinematics will have, we must rely on some form of numerical derivative for revealing possible trends. Since the issues with the 3-point Lagrangian have been highlighted in Section 3, we shall opt instead to implement the Savitzky-Golay filter (Savitzky & Golay, 1964). This is a form of local polynomial regression of chosen degree of smoothing polynomial, and of chosen order to produce smoothed first order, second order, etc., derivatives of the signal. The number of data points either side of the case point to be included in the filter is also specified. So for treating the distance-time data of CMEs and coronal waves, the Savitzky-Golay filter is a better method for smoothing small-scale noise while still revealing the true kinematic profiles. This is illustrated in Figure 8 for the sim-

ulated non-constant acceleration profile, with the residuals resampled with replacement as per the bootstrapping technique described above and demonstrated in Figures 6 and 7. For this case the neighboring 3 points to the left and right of each datapoint were considered. Since it is a form of “moving window averaging”, slight biases may be introduced at local maxima and minima where the function value can be reduced, but its implementation still proves more robust than the standard 3-point Lagrangian at smoothing the scatter while still revealing the overall trend. Note that the residuals can be seen to scatter somewhat randomly, as desired (bottom panel of Figure 8). Also, for this case-study it is important to note how the scatter at the endpoints gives the impression of a decreasing velocity which the Savitzky-Golay filter faithfully reproduces even though we know it’s not how the model is behaving. This is akin to how the intensity of a CME or coronal wave often lies too close to the background intensity at such distances, that it is lost to the noise and the measured profile falls off. This alludes to considerations that must be made when dealing with automated systems of kinematic determination, whereby the algorithmic limitations can introduce systematic biases not accounted for in the derived kinematics and associated uncertainties. This is discussed further in the next section.

5. Case Studies

In this section some examples of real data are presented as case studies for deriving the CME and coronal wave kinematics in light of the discussion of the previous sections.

5.1. CME Kinematics

First we shall revisit a CME studied by Byrne et al. (2009), that was observed by LASCO on 2000 January 2. In that study, the CME front edge was detected via multiscale methods (the basis of the CORIMP CME catalogue) and characterized with an ellipse-fit that was used to track changes to the CME front over time. The apex of the fit (furthest distance from Sun-centre) in each frame was measured, and a height-time profile produced. This allowed an investigation into the kinematics of the event, derived using the 3-point Lagrangian method and associated error propagation formulation (via DERIV.PRO and DERIVSIG.PRO in IDL). However, as has been outlined in the preceding sections, this formulation is somewhat redundant for such a small sample size, and so a new method is applied to test the validity of the analysis.

The method chosen, and deemed most appropriate from our investigations in this paper, is that of the Savitzky-Golay filter and bootstrapping technique. The top panel of Figure 9 shows the height-time plot of the CME (the plus symbols), the resampled residuals (in red) after applying the Savitzky-Golay filter, and corresponding median, interquartile range, and upper and lower fences on the bootstrapped data (blue dashed lines). The middle and bottom panels show the derived velocity and acceleration profiles. An important point to note is that a priori knowledge about the eruptive events and the manner in which they are tracked, must be called upon when interpreting the derived kinematic profiles. Specifically for this example, it is realized that the CME detection and characterization towards the outer edge of the C3 field-of-view is less reliable

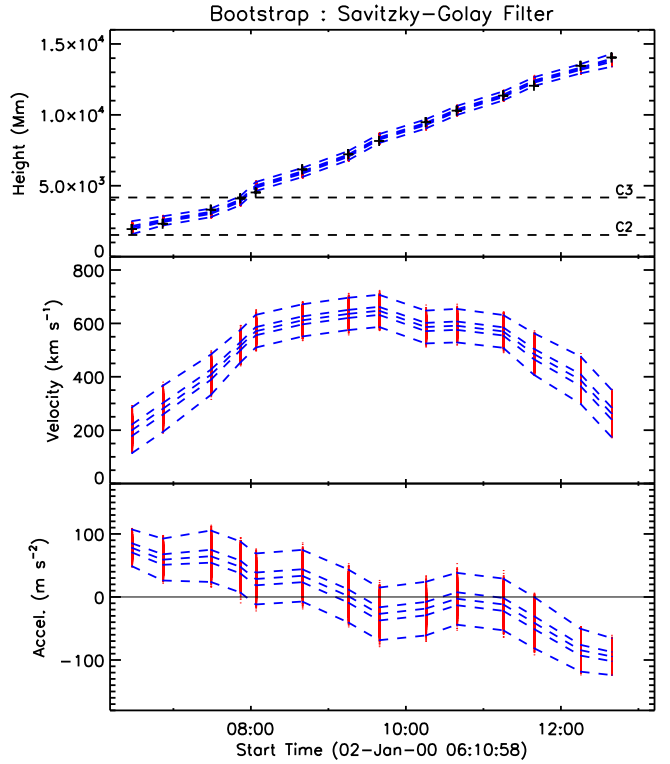


Fig. 9. The bootstrapped Savitzky-Golay filter method applied to a real CME data case revisited from Byrne et al. 2009. The top panel shows the height-time measurements (plus symbols), the resampled residuals (red points), and the median, interquartile range, and upper and lower fences (blue dashed lines). The middle and bottom panels show the corresponding velocity and acceleration profiles.

and prone to bias the measurements to lower heights. This explains the decrease in velocity, and negative acceleration, that is derived, while still being able to reliably quantify the early velocity increase, and high acceleration, of the CME onset (where the detection and tracking is most robust).

Next we shall investigate a CME that occurred on 2011 January 2, as a case-study from the newly developed CORIMP CME catalogue. The height-time points are measured at 1 degree intervals across the angular span of the event as it moves through the corona in time (see top of Figure 10). The Savitzky-Golay filer is then applied to each of these angular slices across the CME, at a chosen window-size of 6 data points (3 neighboring points either side of the datapoint in question) and the corresponding first and second order derivatives of the fit are determined (to reveal the spread of velocity and acceleration points in the middle and bottom plots of Figure 10). Since a spread of measurements across the CME can be determined in these cases, the sample size is therefore larger and the spread is treated as the range of variation in the kinematics without necessarily requiring bootstrap methods to be employed. The implication here is that any variation in CME speeds that may result from the expansion of the ejecta across the plane-of-sky, should provide a distribution of kinematics that is centered on the motion of the bulk of the CME (as opposed to the relatively slower moving flanks of the CME). In essence, this provides a solution space of CME kinematics that is based

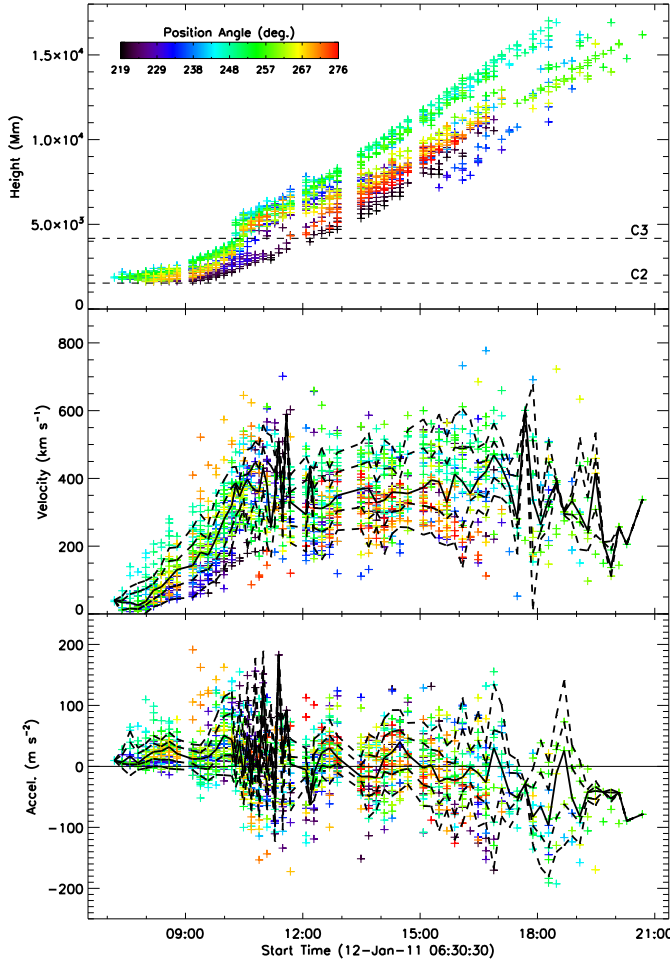


Fig. 10. The Savitzky-Golay filter applied to the automated CORIMP CME detection and tracking of an event observed on 2011 January 12. The top panel shows the height-time measurements across the angular range of the CME (indicated by the color bar). The middle and bottom panels show the derived velocity and acceleration profiles, with the median (solid line), interquartile range (inner dashed lines) and upper and lower fences (outer dashed lines) over plotted on the data.

purely on the distribution of CME height-time measurements. Additional bootstrapping is not necessary at this point since a specific model is not being tested, nor would any algorithmic bias that may have occurred be overcome, e.g. if the CME detection is lost to the background or a false detection contaminates the measurements. However if a user of the catalogue has a specific model that they wish to test, then a bootstrapping procedure and residual analysis would be of use, as demonstrated in Section 4. For the spread of CME kinematic measurements in Figure 10, the median, interquartile range, and upper and lower fences, are determined in order to characterize the significance of the range of velocity and acceleration points. This allows the underlying trend of the data to be inspected, revealing an initial acceleration of approximately 20 m s^{-2} up to a constant velocity of approximately 400 km s^{-1} . Large scatter can occur at the crossover of the two fields-of-view, and at the out edge of the field-of-view.

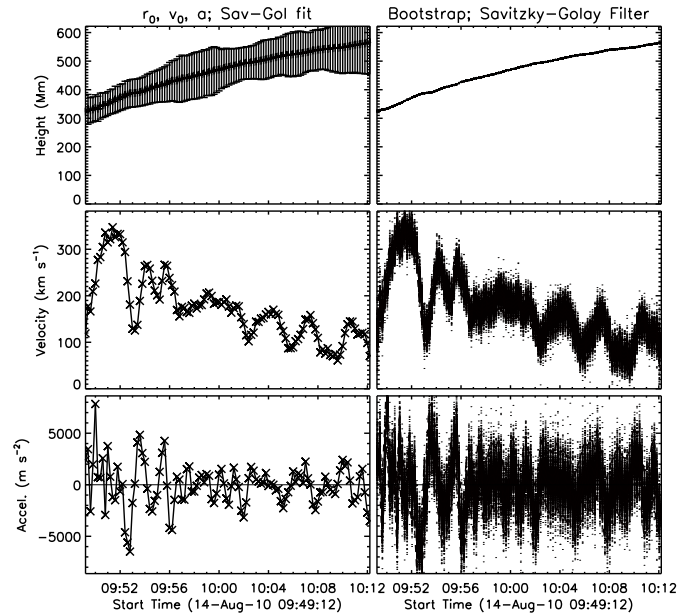


Fig. 11. The bootstrapped Savitzky-Golay filter method applied to a real wave data case. Note the errorbars need work!!!

The ability also exists to choose any individual position angle for investigation, such as the central position angle that may correspond to the maximum speed of the CME. For example, the position angles around 250° here, indicate speeds up to approximately 500 km s^{-1} , so for these specific height-time measurements a model may be fit and a bootstrapping technique used to provide a confidence interval for testing the goodness-of-fit. Thus the output produced from this treatment of the kinematics greatly improves the ability to study CME dynamics.

5.2. Coronal wave kinematics

6. Conclusions

We have demonstrated the unreliability of some common approaches to studying the kinematics of solar eruptive events, namely CMEs and coronal waves. The dynamics of these phenomena are of great consequence to understanding the physics governing their eruption and propagation, and so the caveats and drawbacks of traditional numerical techniques for deriving their velocities and accelerations have been highlighted and efforts to overcome them discussed. Of particular interest is the counter-intuitive behavior of the error propagation in the standard 3-point Lagrangian interpolation, due predominantly to its inverse dependence on the observing cadence. And it is also shown how strongly affected it can be by noise levels akin to those found in the datasets of these solar eruptive events. Therefore, we suggest the use of bootstrapping techniques when dealing with the small sample sizes of these events, and demonstrate both their ease of implementation, and usefulness in measuring the confidence intervals on fit parameters. This is crucial for determining the appropriateness of any chosen theoretical model seeking to characterize the physics

of their motion. When used in conjunction with residual analysis, a robust estimate of the goodness-of-fit can be obtained. Thus the issues of traditional numerical differencing techniques and error propagation are overcome.

An important point to note on this, is that a priori knowledge must still play a large part in the interpretation of such kinematics analyses. This is shown to be especially true for cases where the measurements may have an inherent bias due to observational and/or algorithmic limitations, such as at the outer edges of the coronagraph fields-of-view for a CME, or the intensity limit of a coronal wave on disk. Thus the significance attributed to the kinematic profile must still be interpreted with care, but all other sources of misinterpretation have been reduced via these methods.

Acknowledgements. This work is supported by SHINE grant 0962716 and NASA grant NNX08AJ07G to the Institute for Astronomy. The SOHO/LASCO data used here are produced by a consortium of the Naval Research Laboratory (USA), Max-Planck-Institut fuer Aeronomie (Germany), Laboratoire d'Astromie (France), and the University of Birmingham (UK). SOHO is a project of international cooperation between ESA and NASA. The STEREO/SECCHI project is an international consortium of the Naval Research Laboratory (USA), Lockheed Martin Solar and Astrophysics Lab (USA), NASA Goddard Space Flight Center (USA), Rutherford Appleton Laboratory (UK), University of Birmingham (UK), Max-Planck-Institut fuer Sonnen-systemforschung (Germany), Centre Spatial de Liege (Belgium), Institut d'Optique Theorique et Appliquee (France), and Institut d'Astrophysique Spatiale (France).

References

- Byrne, J. P., Gallagher, P. T., McAteer, R. T. J., & Young, C. A. 2009, *A&A*, 495, 325
 Byrne, J. P., Maloney, S. A., McAteer, R. T. J., Refojo, J. M., & Gallagher, P. T. 2010, *Nature Communications*, 1
 Byrne, J. P., Morgan, H., Habbal, S. R., & Gallagher, P. T. 2012, *ApJ*, 752, 145
 Chen, P. F., & Wu, Y. 2011, *ApJ*, 732, L20
 Chernick, M. 1999, *Bootstrap methods: A practitioner's guide* (New York: Wiley)
 Efron, B. 1979, *Ann. Stat.*
 Efron, B., & Tibshirani, R. J. 1994, *An Introduction to the Bootstrap* (Chapman & Hall/CRC)
 Gallagher, P. T., & Long, D. M. 2011, *Space Sci. Rev.*, 158, 365
 Howard, T., ed. 2011, *Astrophysics and Space Science Library*, Vol. 376, Coronal Mass Ejections%
 Illing, R. M. E., & Hundhausen, A. J. 1985, *J. Geophys. Res.*, 90, 275
 Lin, C., Gallagher, P. T., & Raftery, C. L. 2010, *A&A*, 516, A44+
 Long, D. M., Gallagher, P. T., McAteer, R. T. J., & Bloomfield, D. S. 2008, *ApJ*, 680, L81
 —. 2011, *A&A*, 531, A42
 Ma, S., Wills-Davey, M. J., Lin, J., et al. 2009, *ApJ*, 707, 503
 Morgan, H., Byrne, J. P., & Habbal, S. R. 2012, *ApJ*, 752, 144
 Patsourakos, S., & Vourlidas, A. 2012, *Sol. Phys.*, 93
 Podladchikova, O., Vuets, A., Leontiev, P., & van der Linden, R. A. M. 2012, *Sol. Phys.*, 276, 479
 Prangé, R., Pallier, L., Hansen, K. C., et al. 2004, *Nature*, 432, 78
 Savitzky, A., & Golay, M. 1964, *Analytical Chemistry*, 36, 1627
 Schrijver, C. J., Aulanier, G., Title, A. M., Pariat, E., & Delannée, C. 2011, *ApJ*, 738, 167
 Schrijver, C. J., Elmore, C., Kliem, B., Török, T., & Title, A. M. 2008, *ApJ*, 674, 586
 Schwenn, R., dal Lago, A., Huttunen, E., & Gonzalez, W. D. 2005, *Annales Geophysicae*, 23, 1033
 Shen, Y., & Liu, Y. 2012, *ApJ*, 754, 7
 Thompson, B. J., & Myers, D. C. 2009, *ApJS*, 183, 225
 Veronig, A. M., Muhr, N., Kienreich, I. W., Temmer, M., & Vršnak, B. 2010, *ApJ*, 716, L57
 Warmuth, A., & Mann, G. 2011, *A&A*, 532, A151
 Webb, D. F., & Howard, T. A. 2012, *Living Reviews in Solar Physics*, 9, 3
 Wen, Y., Maia, D. J. F., & Wang, J. 2007, *ApJ*, 657, 1117
 Yashiro, S., Gopalswamy, N., Michalek, G., et al. 2004, *Journal of Geophysical Research (Space Physics)*, 109, 7105
 Zheng, R., Jiang, Y., Yang, J., et al. 2012, *ApJ*, 753, 112